Journal of Magnetic Resonance **143,** 120–135 (2000)
doi:10.1006/jmre.1999.1967, available online at http://www.idealibrary.com on IDEAL®

Spin Dynamics of Carr–Purcell–Meiboom–Gill-like Sequences in Grossly Inhomogeneous B_0 and B_1 Fields and Application to NMR Well Logging

M. D. Hürlimann and D. D. Griffin

Schlumberger-Doll Research, Ridgefield, Connecticut 06877-4108

Received July 13, 1999; revised October 15, 1999

The spin dynamics for Carr–Purcell–Meiboom–Gill-like sequences is analyzed in grossly inhomogeneous B_0 and B_1 fields. This problem is important for many applications, especially when the bandwidth of the signal is excitation limited. Examples include stray-field NMR or inside-out NMR probes used in well logging. The amplitudes of the first few echoes exhibit a characteristic transient behavior but quickly approach a smooth asymptotic behavior. For simple Hamiltonians without scalar or dipolar couplings, the evolution of a refocusing subcycle for a given isochromat is described by a rotation. Simple expressions for the signal of the *N*th echo are derived in terms of these effective rotations that have a simple geometrical interpretation. It is shown that the asymptotic behavior is controlled by the direction of the axis of these effective rotations and the signal is dominated by magnetization "spin-locked" to the rotation axis. The phase of the signal is independent of the details of the field inhomogeneities. Relaxation in inhomogeneous fields leads to a signal decay that is in general nonexponential with an initial decay rate that is a weighted sum of T_1^{-1} and T_2^{-1}. At long times, the echo amplitudes decay to a finite value. Phase cycling eliminates this offset. The effect of diffusion is also studied. This analysis has been applied to an inside-out NMR well logging apparatus. Good quantitative agreement is found between measurements and calculations that are based on the measured B_0 and B_1 field maps. © 2000 Academic Press

Key Words: **inhomogeneous fields; CPMG; relaxation; diffusion; well logging.**

1. INTRODUCTION

In standard NMR measurements, great care is taken to apply a static magnetic field, $\mathbf{B}_0$, and an RF field, $\mathbf{B}_1$, that are as homogeneous as possible over the sample volume. However, there are a number of applications where NMR measurements are performed in grossly inhomogeneous fields. This includes applications where the sample is outside the apparatus, such as in NMR well logging (*1*) or in materials testing with portable NMR surface scanners (*2, 3*). In stray-field NMR (*4*), the sample is deliberately placed at a spot where the static magnetic field is very inhomogeneous. When surface coils are used in MRI, the RF field at the sample is highly nonuniform. Another application is NQR on polycrystalline materials, as used, for instance, in the detection of explosives or narcotics (*5, 6*). In this case, the effective RF field varies from crystallite to crystallite, because only the component of the RF field along the relevant axis of the electric field gradient tensor is effective.

Here we study the spin dynamics in both inhomogeneous static and RF fields. We concentrate on multipulse sequences such as the Carr–Purcell–Meiboom–Gill (CPMG) sequence (*7, 8*), where the magnetization is refocused repeatedly and measured stroboscopically at constant time intervals.

The paper is organized as follows: In Section 2, we formulate the general problem of spin dynamics in grossly inhomogeneous fields. The general expression for the signal of the *N*th echo is derived. We analyze the spin dynamics in terms of effective rotations that represent the spin dynamics of an entire refocusing subcycle. Special attention is given to the axis of these rotations. In Section 3, we apply the general analysis to the CPMG sequence. Simple expressions for the asymptotic signal as a function of offset and detuning parameters are given. Relaxation is examined in Section 4. Results for the initial decay rate in terms of $1/T_1$ and $1/T_2$ are derived. Simple expressions for signal offsets at long time are obtained for $T_1 = T_2$. In Section 5, we apply the analysis of the previous sections to the case of an NMR logging apparatus used in oilfield applications. The B_0 and B_1 fields were mapped and calculations directly compared with measurements. Diffusion effects are discussed in Section 6.

In previous work, Vold *et al.* (*9*) studied experimentally the effect of imperfect pulses and frequency offsets on the relaxation times measured with the CPMG sequence. Our analytical results are in agreement with their observed offsets at long time. Bull (*10*) also studied the magnetization decay observed with the CPMG sequence in inhomogeneous fields. He obtained analytical results for some special cases that were confirmed experimentally and are in agreement with our results. Benson and McDonald (*11, 12*) studied the amplitude modulation of the first few echoes in a constant gradient for stray-field applications, both theoretically and experimentally. Goel-

1090-7807/00 $35.00
Copyright © 2000 by Academic Press
All rights of reproduction in any form reserved.

man and Prammer (*13*) analyzed a different well logging apparatus. Analytical results were obtained for the first few echoes and numerical simulations were used to investigate the effects of inhomogeneous fields on the measured relaxation times. Bain and Randall (*14*) analyzed two sequences, 90°_x–$(90^\circ_y)^n$ and 90°_x–$(90^\circ_x)^n$, in inhomogeneous fields. Assuming delta-function RF pulses, they calculated the echo amplitudes of the first few echoes and found that they oscillate and approach different limits. Our approach in this paper gives a simple geometrical interpretation for this observation and allows one to generalize the calculation to include finite pulse width and relaxation.

2. SPIN DYNAMICS IN INHOMOGENEOUS FIELDS

We assume that the spin dynamics is solely determined by the Larmor precession in the applied static field $\mathbf{B}_0(\mathbf{r})$ and the effects of the RF field $\mathbf{B}_1(\mathbf{r}, t)$. Effects of relaxation and diffusion are considered later. We further assume that $|\mathbf{B}_0(\mathbf{r})| \gg |\mathbf{B}_1(\mathbf{r}, t)|$. In this case, we only have to consider the component of the RF field $\mathbf{B}_1$ that is circularly polarized and orthogonal to $\mathbf{B}_0(\mathbf{r})$. This component has the magnitude

$$\mathbf{B}_{1c} = \frac{1}{2}\left[\mathbf{B}_1(\mathbf{r}) - \mathbf{B}_0(\mathbf{r})\frac{\mathbf{B}_1(\mathbf{r})\cdot\mathbf{B}_0(\mathbf{r})}{\mathbf{B}_0(\mathbf{r})\cdot\mathbf{B}_0(\mathbf{r})}\right]. \qquad [1]$$

The spin dynamics depends on the two vector fields $\mathbf{B}_0$ and $\mathbf{B}_{1c}$ only through two scalar quantities, $\Delta\omega_0$ and ω_1. $\Delta\omega_0$ is the offset of the RF frequency ω_{RF} from the local Larmor frequency, $\gamma|\mathbf{B}_0|$:

$$\Delta\omega_0 \equiv (\omega_{RF} - \gamma|\mathbf{B}_0|). \qquad [2]$$

On resonance, $\Delta\omega_0 = 0$. Note that we use the same sign convention as in (*15*). The second frequency, ω_1, measures the amplitude of the RF pulse and is defined by

$$-\gamma B_{1c}(t) = \omega_1 \cos(\omega_{RF} t + \phi). \qquad [3]$$

Here ϕ is the phase of the RF pulse. With this notation, the Hamiltonian in the rotating frame of the RF frequency becomes

$$\mathcal{H} = \sum_{k=1}^{N} \{\Delta\omega_{0,k} I_{z,k} + \omega_{1,k}(t)(\cos\phi I_{x,k} + \sin\phi I_{y,k})\}. \qquad [4]$$

2.1. General Expression for Signal

The in- and out-of-phase voltage induced in the coil from a sample in grossly inhomogeneous fields can be written as (*16, 17*)

$$V_{x,y}(t) = \frac{2\chi}{\mu_0}\int d\mathbf{r}\Phi(\mathbf{r})\, B_0^2(\mathbf{r})\, \frac{\omega_1(\mathbf{r})}{I}\, F(\Delta\omega_0(\mathbf{r}))m_{x,y}(\mathbf{r}t). \qquad [5]$$

Here χ is the nuclear susceptibility. The quantity $m_{x,y}(\mathbf{r}, t)$ is the local transverse magnetization at point $\mathbf{r}$ and time t, normalized to the thermal longitudinal magnetization, $M_0(\mathbf{r}) = \chi/\mu_0\, B_0(\mathbf{r})$. For water at room temperature, the nuclear susceptibility, χ, is $\chi = 4.04 \times 10^{-9}$ in MKS units. $F(\Delta\omega_0)$ is the frequency response of the detection system, including the coil response and any hardware or software filters. I is the current needed in the coil to give raise to $\omega_1(\mathbf{r})$ in the sample. By reciprocity, the factor of $\omega_1(\mathbf{r})/I$ gives then the efficiency of the coil to detect magnetization at a point **r.** In Eq. [5], one factor of B_0 stems from the Boltzmann factor; the other comes from Faraday's law. We have included a term $\Phi(\mathbf{r})$ to denote the variations in the local density of spins. In porous media, $\Phi(\mathbf{r})$ corresponds to the local porosity.

For many applications, it is convenient to replace the three-dimensional integral over $\mathbf{r}$ in Eq. [5] by a two-dimensional integral over $\Delta\omega_0$ and ω_1. A distribution function, $f(\Delta\omega_0, \omega_1)$, is determined from the field maps $B_0(\mathbf{r})$ and $B_1(\mathbf{r})$ (and the porosity map $\Phi(\mathbf{r})$), such that $f(\Delta\omega_0, \omega_1)\delta\Delta\omega_0\delta\omega_1$ equals the number of spins with $\Delta\omega_0 \pm \delta\Delta\omega_0$ and $\omega_1 \pm \delta\omega_1$, multiplied by the coil efficiency factor $\omega_1(\mathbf{r})/I$. With this distribution function, the expression for the signal, Eq. [5], becomes

$$\begin{aligned} V_{x,y}(t) &= \frac{2\chi}{\mu_0}\int\int d\Delta\omega_0 d\omega_1 f(\Delta\omega_0, \omega_1)(\omega_{RF} - \Delta\omega_0)^2 \\ &\quad \times F(\Delta\omega_0)m_{x,y}(\Delta\omega_0, \omega_1) \\ &\simeq \frac{2\chi}{\mu_0}\int\int d\Delta\omega_0 d\omega_1 f(\Delta\omega_0, \omega_1)\omega_{RF}^2 \\ &\quad \times F(\Delta\omega_0)m_{x,y}(\Delta\omega_0, \omega_1). \end{aligned} \qquad [6]$$

Here we have used the fact that $|\mathbf{B}_0| \gg |\mathbf{B}_1|$. Note that this description as a two-dimensional integral over $\Delta\omega_0$ and ω_1 is possible as long as the signal depends only on the local values of the fields. This is not the case if motion during the measurement is important, for instance, due to diffusion, flow, or movement of the NMR instrument with respect to the sample.

2.2. CPMG-like Sequences in Grossly Inhomogeneous Fields

In the absence of relaxation, the normalized magnetization $m(\mathbf{r}, t)$ is a unit vector, initially pointing along the local direction of the static field. It is best to describe the spin dynamics in local rotating frames that rotate with the carrier frequency ω_{RF} around the local direction of $\mathbf{B}_0(\mathbf{r})$. At each point **r,** the coordinate system of the rotating frame is chosen

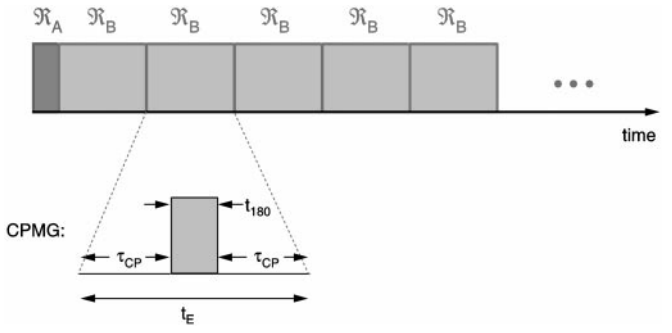

FIG. 1. Schematic pulse sequence: The general pulse sequence is composed of an initial excitation sequence, represented by a rotation $\mathcal{R}_{\mathcal{A}}$, followed by a large number of refocusing cycles, represented by rotations $\mathcal{R}_{\mathcal{B}}$. The signal forms at the end of each refocusing cycle. In the CPMG pulse sequence, the excitation sequence consists of an RF pulse of duration t_{90}. The refocusing cycle consists of a period of free precession of duration $\tau_{CP} = (t_E - t_{180})/2$, an RF pulse of duration t_{180}, followed by another identical period of free precession.

such that the $\hat{z}$ axis is pointing along the $\mathbf{B}_0$ field and the $\hat{x}$ axis is pointing along the local direction of $\mathbf{B}_{1c}$ when $\phi = 0$. For our calculation, we assume that the same RF coil is used as transmitter and receiver.

In this rotating frame the spin dynamics consists of consecutive rotations $\mathcal{R}$. The axis $\hat{n}$ and the nutation frequency Ω characterizing the rotations during the RF pulses are determined by the applied RF field strength and the detuning:

$$\Omega = \sqrt{\Delta\omega_0^2 + \omega_1^2} \qquad [7]$$

$$\hat{n} = \frac{\omega_1}{\Omega}[\cos(\phi)\hat{x} + \sin(\phi)\hat{y}] + \frac{\Delta\omega_0}{\Omega}\hat{z}. \qquad [8]$$

Between the RF pulses, $\omega_1 = 0$ and the magnetization evolves around the $\hat{z}$-axis:

$$[m_x + im_y](\mathbf{r}, t) = \exp\{i\Delta\omega_0(\mathbf{r})(t - t_0)\}[m_x + im_y](\mathbf{r}, t_0). \qquad [9]$$

In grossly inhomogeneous fields, this leads to fast dephasing of the overall magnetization, and refocusing pulses are used for rephasing. We consider here generalized CPMG-like sequences of the form shown in Fig. 1. After the initial subsequence $\mathcal{A}$, used to excite the spins, identical subsequences $\mathcal{B}$ are applied repeatedly and the echoes are formed at the end of each cycle of $\mathcal{B}$. In general, the subsequences $\mathcal{A}$ and $\mathcal{B}$ can consist of any number of RF pulses and sweeps and periods without any applied RF. The refocusing cycle is assumed to be repeated typically several hundred to thousand times. In oilfield logging applications, this is necessary to determine relaxation times that can span three orders of magnitude in time. In the standard CPMG sequence, $\mathcal{A}$ consists of a single 90° pulse and $\mathcal{B}$ is composed of three periods: an initial period τ_{cp} without RF, a 180° pulse, and another period τ_{cp} without RF. With this notation, the echo spacing t_E is $t_E = 2\tau_{cp} + t_{180}$.

2.3. Overall Rotation for Refocusing Cycle

The evolution over a single subcycle $\mathcal{B}$ consists of consecutive rotations. In the absence of relaxation and with our assumptions made before, this evolution can always be described by a single, overall rotation $\mathcal{R}_{\mathcal{B}}$. The overall rotation $\mathcal{R}_{\mathcal{B}}$ is characterized by an axis of rotation, $\hat{n}_{\mathcal{B}}$, and an angle of rotation, $\alpha_{\mathcal{B}}$. Similarly, we can describe the effect of the subcycle $\mathcal{A}$ by the net rotation $\mathcal{R}_{\mathcal{A}}$. The overall evolution between the initial condition and the end of the Nth cycle of $\mathcal{B}$, the Nth echo, is then completely determined by

$$\mathbf{m}_N = [\mathcal{R}_{\mathcal{B}}(\hat{n}_{\mathcal{B}}, \alpha_{\mathcal{B}})]^N \mathcal{R}_{\mathcal{A}}\{\hat{z}\} = \mathcal{R}_{\mathcal{B}}(\hat{n}_{\mathcal{B}}, N\alpha_{\mathcal{B}})\mathcal{R}_{\mathcal{A}}\{\hat{z}\}. \qquad [10]$$

It is useful to rewrite this as

$$\mathbf{m}_N = \hat{n}_{\mathcal{B}}(\hat{n}_{\mathcal{B}} \cdot \mathcal{R}_{\mathcal{A}}\{\hat{z}\}) + [\mathcal{R}_{\mathcal{A}}\{\hat{z}\} - \hat{n}_{\mathcal{B}}(\hat{n}_{\mathcal{B}} \cdot \mathcal{R}_{\mathcal{A}}\{\hat{z}\})] \times \cos(N\alpha_{\mathcal{B}}) + (\hat{n}_{\mathcal{B}} \times \mathcal{R}_{\mathcal{A}}\{\hat{z}\})\sin(N\alpha_{\mathcal{B}}). \qquad [11]$$

The first term does not depend on the echo number N, whereas the second and third terms oscillate with a frequency $\alpha_{\mathcal{B}}$. This frequency depends on $\Delta\omega_0$ and ω_1, which are assumed here to have a wide range of values. Therefore, only the first term adds coherently from echo to echo.

2.4. Asymptotic Signal

Since the signal is obtained by integrating the contributions from all spins, the second and third terms of Eq. [11] are only important for the early echoes. For a sufficiently high number of echoes, the signal will be dominated by the first term; the other two terms tend to average out.

This statement implicitly assumes that $\alpha_{\mathcal{B}} \neq 0$. There are special points in the $\Delta\omega_0 - \omega_1$ plane where $\mathcal{R}_{\mathcal{B}}$ is the identity operation with $\alpha_{\mathcal{B}} = 0$. For these points, the second and third terms in Eq. [11] will not average out. However, in inhomogeneous fields, the contribution from these points is typically very small and this complication can be neglected in most cases.

The first term in Eq. [11] can be thought of as a generalized form of spin locking. The spins are locked not to the actual RF field with axis $(\omega_1/\Omega)\hat{y} + (\Delta\omega_0/\Omega)\hat{z}$, but to the effective axis $\hat{n}_{\mathcal{B}}$ that includes the effect of free precession between the pulses. At long enough times, only the magnetization locked to $\hat{n}_{\mathcal{B}}$ survives; the other terms give rise to a transient. In another language (*10*), $\hat{n}_{\mathcal{B}}$ is the eigenvector of the operator $\mathcal{B}$ with the eigenvalue 1. The other two eigenvalues are complex. At long time, the asymptotic signal is then given by

$$V_{x,y}^{\infty}(t) = \frac{2\chi}{\mu_0}\int\int d\Delta\omega_0 d\omega_1 f(\Delta\omega_0,\ \omega_1)(\omega_{\mathrm{RF}} - \Delta\omega_0)^2 \times F(\Delta\omega_0)[(\hat{x} + i\hat{y})\cdot\hat{n}_{\mathcal{B}}](\hat{n}_{\mathcal{B}}\cdot\mathcal{R}_{\mathcal{A}}\{\hat{z}\}). \quad [12]$$

In general, the largest signal is generated with refocusing sequences $\mathcal{B}$ for which the effective axis of rotation, $\hat{n}_{\mathcal{B}}$, points in the same direction in the x–y plane over as large a range of $\Delta\omega_0$ and ω_1 as possible. Such a refocusing sequence should be combined with an initial pulse cycle $\mathcal{A}$ that rotates the vector $\hat{z}$ onto $\hat{n}_{\mathcal{B}}$.

Note that the angle $\alpha_{\mathcal{B}}$ does not enter the optimization directly (it only affects the transient signal at early times).

3. ANALYSIS OF CPMG SEQUENCE IN INHOMOGENEOUS FIELDS

In the standard CPMG sequence (*7, 8*), the excitation cycle $\mathcal{A}$ consists of a single $\pi/2$ pulse and the refocusing cycle $\mathcal{B}$ consists of three intervals: an interval τ_{cp} of free precession, followed by a π pulse applied along the $\hat{y}$ axis of duration t_{180}, and another interval τ_{cp} of free precession (see Fig. 1).

Modified Carr–Purcell sequences have been introduced where the phase of the refocusing pulse is cycled within the sequence (*18–21*). Denoting $\mathcal{R}_{\mathcal{B}k}$ the evolution of the kth refocusing cycle and assuming that the phase cycle has N elements, we can analyze these modified sequences with the same approach as discussed before. There are N different types of echoes and for the jth type, the refocusing rotation $\mathcal{R}_{\mathcal{B}}$ has to be replaced by $\mathcal{R}_{\mathcal{B}} \rightarrow \mathcal{R}_{\mathcal{B}j-1}\ldots\mathcal{R}_{\mathcal{B}1}\mathcal{R}_{\mathcal{B}N}\ldots\mathcal{R}_{\mathcal{B}j}$ and the excitation cycle $\mathcal{R}_{\mathcal{A}}$ by $\mathcal{R}_{\mathcal{A}} \rightarrow \mathcal{R}_{\mathcal{B}j-1}\ldots\mathcal{R}_{\mathcal{B}1}\mathcal{R}_{\mathcal{A}}$. For our application discussed in Section 5, we found no benefit in using these modified sequences and we concentrate here on the standard CPMG sequence.

To calculate the axis $\hat{n}_{\mathcal{B}}$ and angle $\alpha_{\mathcal{B}}$ of the overall rotation resulting from several consecutive rotations, we use the expressions given by Counsell *et al.* (*22*). A rotation characterized by $(\hat{n}_1,\ \alpha_1)$, followed by a second rotation characterized by $(\hat{n}_2,\ \alpha_2)$, is described by a net rotation around an axis $\hat{n}_{12}$ and an angle α_{12} given by

$$\cos\left(\frac{\alpha_{12}}{2}\right) = \cos\left(\frac{\alpha_1}{2}\right)\cos\left(\frac{\alpha_2}{2}\right) - \sin\left(\frac{\alpha_1}{2}\right)\sin\left(\frac{\alpha_2}{2}\right)\hat{n}_1\cdot\hat{n}_2 \quad [13]$$

$$\sin\left(\frac{\alpha_{12}}{2}\right)\hat{n}_{12} = \sin\left(\frac{\alpha_1}{2}\right)\cos\left(\frac{\alpha_2}{2}\right)\hat{n}_1 + \cos\left(\frac{\alpha_1}{2}\right)\sin\left(\frac{\alpha_2}{2}\right)\hat{n}_2 - \sin\left(\frac{\alpha_1}{2}\right)\sin\left(\frac{\alpha_2}{2}\right)\hat{n}_1\times\hat{n}_2. \quad [14]$$

3.1. Refocusing Cycle $\mathcal{B}$ for CPMG Sequence

For arbitrary offsets in $\Delta\omega_0$ and ω_1, the rotation for the refocusing cycle, $\mathcal{R}_{\mathcal{B}}$, becomes

$$\mathcal{R}_{\mathcal{B}} = \mathcal{R}(\hat{z},\ \Delta\omega_0\tau_{\mathrm{cp}}) \times \mathcal{R}\left(\left(\frac{\omega_1}{\Omega}\hat{y} + \frac{\Delta\omega_0}{\Omega}\hat{z}\right),\ \Omega t_{180}\right)\mathcal{R}(\hat{z},\ \Delta\omega_0\tau_{\mathrm{cp}}). \quad [15]$$

For all symmetrical composites of the form $\mathcal{R}_c = \mathcal{R}(\hat{n}_1,\ \alpha_1)\mathcal{R}(\hat{n}_2,\ \alpha_2)\mathcal{R}(\hat{n}_1,\ \alpha_1)$, the axis of the composite rotation lies in the plane spanned by $(\hat{n}_1,\ \hat{n}_2)$. This implies that for the CPMG sequence, the axis $\hat{n}_{\mathcal{B}}$ always lies in the $(\hat{y},\ \hat{z})$ plane and $\hat{n}_{\mathcal{B}}\cdot\hat{x} = 0$. At long times, the signal at the peak of the echo has therefore only a y-component and no x-component, independent of the profile of B_0 or B_1.

This analysis is based on rectangular RF pulses. If the RF pulses have finite rise and fall times, the temporal symmetry is in general broken. Even if the pulses have a short rise time, the tuned circuit of the transmitter coil will cause "phase glitches" in the applied field B_1, especially in probes with high Q (*23, 24*). Both of these effects will lead to a small x-component in the axis of the composite rotation. This complication is neglected below.

It is convenient to use the following abbreviations: $n_x \equiv \hat{n}_{\mathcal{B}}\cdot\hat{x}$; $n_y \equiv \hat{n}_{\mathcal{B}}\cdot\hat{y}$; $n_z \equiv \hat{n}_{\mathcal{B}}\cdot\hat{z}$. For rectangular pulses, the following results are obtained:

$$n_y = \hat{n}_{\mathcal{B}}\cdot\hat{y} = \frac{\omega_1}{\Omega} \times \frac{\sin\beta_2}{\left\{\left[\frac{\omega_1}{\Omega}\sin\beta_2\right]^2 + \left[\sin\beta_1\cos\beta_2 + \frac{\Delta\omega_0}{\Omega}\cos\beta_1\sin\beta_2\right]^2\right\}^{1/2}} \quad [16]$$

$$n_z = \hat{n}_{\mathcal{B}}\cdot\hat{z} = \frac{\sin\beta_1\cos\beta_2 + \frac{\Delta\omega_0}{\Omega}\cos\beta_1\sin\beta_2}{\left\{\left[\frac{\omega_1}{\Omega}\sin\beta_2\right]^2 + \left[\sin\beta_1\cos\beta_2 + \frac{\Delta\omega_0}{\Omega}\cos\beta_1\sin\beta_2\right]^2\right\}^{1/2}} \quad [17]$$

$$\cos\left(\frac{\alpha_{\mathcal{B}}}{2}\right) = \cos\beta_1\cos\beta_2 - \frac{\Delta\omega_0}{\Omega}\sin\beta_1\sin\beta_2, \quad [18]$$

where

$$\beta_1 = \Delta\omega_0\tau_{\mathrm{cp}} \quad [19]$$

$$\beta_2 = \Omega t_{180}/2, \quad [20]$$

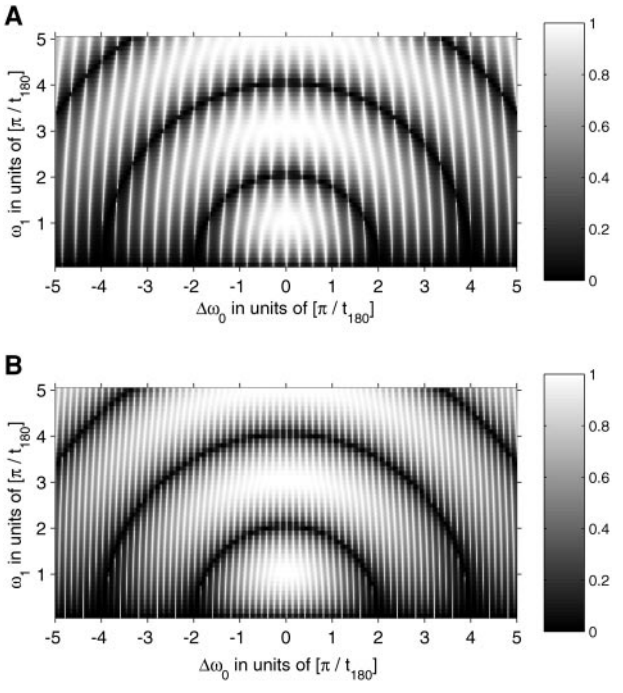

FIG. 2. Component of the axis of the effective rotation describing the refocusing cycle $\mathcal{R}_{\mathcal{B}}$ along the $\hat{y}$ direction, $|n_y|$, for the refocusing cycle of the CPMG sequence as a function of the normalized detuning from the Larmor frequency, $\Delta\omega_0 t_{180}/\pi$, and the normalized RF field strength, $\omega_1 t_{180}/\pi$. The refocusing cycle consists of free precession interval and a nominal $180°|_y$ pulse, followed by another free precession interval. The two figures are for different echo spacings, t_E, or duration of the refocusing cycle. (A) $t_E = 7t_{180}$; (B) $t_E = 15t_{180}$.

and $\Delta\omega_0$, ω_1, and Ω were given in Eqs. [2], [3], and [7], respectively. In these expressions, $0 \leq \alpha_{\mathcal{B}} < 2\pi$. Alternatively, one could choose $n_y \geq 0$, because $(\hat{n}_{\mathcal{B}}, \alpha_{\mathcal{B}})$ and $(-\hat{n}_{\mathcal{B}}, 2\pi - \alpha_{\mathcal{B}})$ describe identical situations. Note that $n_y(-\Delta\omega_0, \omega_1) = n_y(\Delta\omega_0, \omega_1)$, $n_z(-\Delta\omega_0, \omega_1) = -n_z(\Delta\omega_0, \omega_1)$, and $\alpha_{\mathcal{B}}(-\Delta\omega_0, \omega_1) = \alpha_{\mathcal{B}}(\Delta\omega_0, \omega_1)$.

3.1.1. Axis of the effective rotation for the refocusing cycle. In Fig. 2, the y-component of the axis $\hat{n}_{\mathcal{B}}$ describing the refocusing cycle, $|n_y|$, is plotted as a function of $\Delta\omega_0$ and ω_1. In this figure, the units of the frequencies $\Delta\omega_0$ and ω_1 are $\omega_1^0 \equiv \pi/t_{180}$, the nominal value of ω_1 for a 180° pulse on resonance. In these units, the main sweet spot occurs at $(\Delta\omega_0/\omega_1^0, \omega_1/\omega_1^0) = (0, 1)$. Results are shown for two values of $t_E/t_{180} = 7$ and 15.

Figure 2 shows that the axis of the effective rotation is affected by both the pulse strength and the echo spacing. The circular features depend mainly on Ω and scale with the RF field strength. There is a multitude of circles, because on resonance, an odd multiple of the nominal pulse strength ω_1^0 leads again to a 180° pulse modulo 360° pulses. In addition, there are predominately vertical features superimposed on these circular features. These vertical features scale with the inverse of the echo spacing, $1/t_E$.

Quantitatively, the axis of the effective rotation has the following features in the $\Delta\omega_0 - \omega_1$ plane:

- Pure $\hat{z}$-rotations: The dark semicircles correspond to $n_y = 0$, i.e., pure $\hat{z}$-rotations. These lines are described by $(\Delta\omega_0/\omega_1^0)^2 + (\omega_1/\omega_1^0)^2 = (2k)^2$; ($k$ integer). Under this condition, $\Omega t_{180} = k2\pi$, i.e., the RF pulse has no net effect. The overall rotation $\mathcal{R}_{\mathcal{B}}$ is purely a rotation around the $\hat{z}$-axis with an angle $2\Delta\omega_0\tau_{cp}$.
- Pure $\hat{y}$-rotations: In the $\Delta\omega_0 - \omega_1$ plane, there are also lines along which $|n_y| = 1$, i.e., pure $\hat{y}$-rotations. The jth line originates at $(\Delta\omega_0/\omega_1^0, \omega_1/\omega_1^0) = (0, 2j - 1)$ (j integer), and ends at the $\omega_1 = 0$ axis at $(\Delta\omega_0/\omega_1^0, \omega_1/\omega_1^0) = (\pm j\ 2t_{180}/t_E, 0)$. In addition, pure $\hat{y}$-rotations are also obtained along the on-resonance line $\Delta\omega_0 = 0$.
- Identity operation: The lines of pure $\hat{y}$-rotations intersect the lines of pure $\hat{z}$-rotations at special points where the overall rotation $\mathcal{R}_{\mathcal{B}}$ is the identity operation. At these points, the axis of rotation is not uniquely defined and can be chosen in any direction. The kth semicircle of pure $\hat{z}$-rotations is intersected by the jth line of pure $\hat{y}$-rotation if $k < j < k\ t_E/t_{180}$ and it occurs at $(\Delta\omega_0/\omega_1^0, \omega_1/\omega_1^0)_{k,j} = (\pm(j - k)\ t_{180}/\tau_{cp}, \sqrt{(2k)^2 - ((j-k)t_{180}/\tau_{cp})^2})$. In addition, the following points on the axes describe identity operations: $(\Delta\omega_0/\omega_1^0, \omega_1/\omega_1^0) = (\pm j\ 2t_{180}/t_E, 0)$ and $(\Delta\omega_0/\omega_1^0, \omega_1/\omega_1^0) = (0, 2k)$.

3.2. Asymptotic Signal for CPMG Sequence

The asymptotic signal of the CPMG sequence is due to the magnetization that is locked to the composite rotation axis $\hat{n}_{\mathcal{B}}$, as shown in Eq. [12]. At the nominal echo center, this magnetization, normalized to the equilibrium magnetization, can be written as

$$\mathbf{m}_\infty = \hat{n}_{\mathcal{B}}(\hat{n}_{\mathcal{B}} \cdot \mathcal{R}_{\mathcal{A}}\{\hat{z}\}). \qquad [21]$$

We have shown that $\hat{n}_{\mathcal{B}}$ has no x-component. It follows that the asymptotic signal at the nominal echo center is always in the y-channel with $V_x^\infty = 0$. The signal exhibits a pure absorption spectrum, independent of the exact nature of the field inhomogeneities.

For the CPMG sequence, the initial excitation $\mathcal{R}_{\mathcal{A}}\{\hat{z}\}$ is a nominal $90°|_{\pm x}$ pulse on resonance. Meiboom and Gill (*8*) first pointed out that the phase of the initial pulse has to be shifted by 90° with respect to the refocusing pulses. This requirement can be easily understood from Eq. [21]. To obtain the largest signal, the initial pulse has to tip the magnetization in a direction colinear with the axis $\hat{n}_{\mathcal{B}}$, therefore maximizing $(\hat{n}_{\mathcal{B}} \cdot \mathcal{R}_{\mathcal{A}}\{\hat{z}\})$. Without a phase shift between the 90° pulse and the subsequent 180° refocusing pulses, the magnetization is predominantly perpendicular to $\hat{n}_{\mathcal{B}}$ and the asymptotic signal vanishes. The same argument immediately explains the differ-

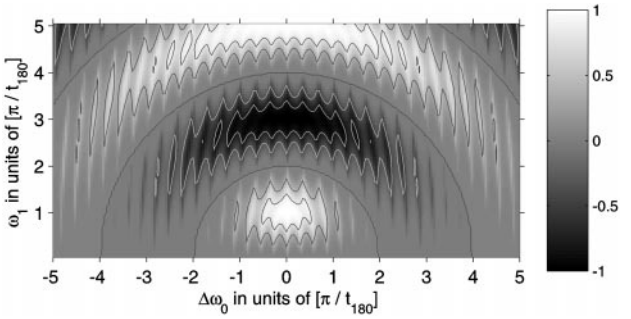

FIG. 3. Normalized asymptotic magnetization for CPMG sequence, $m_{\infty,y}$, as a function of $\Delta\omega_0 t_{180}/\pi$ and $\omega_1 t_{180}/\pi$. The solid lines are contour lines at 0, ± 0.5, and ± 0.9. The echo spacing was set to $t_E = 7t_{180}$.

ence in the asymptotic behavior of the two sequences analyzed by Bain and Randall in (*14*).

For an initial $90°|_{\pm x}$ pulse, the resulting magnetization $\mathcal{R}_{\pm 90x}\{\hat{z}\}$ for arbitrary offsets in B_0 or B_1 is given by

$$\mathcal{R}_{\pm 90x}\{\hat{z}\} = \begin{pmatrix} \pm\dfrac{\Delta\omega_0\omega_1}{\Omega^2}(1-\cos\Omega t_{90}) \\ \mp\dfrac{\omega_1}{\Omega}\sin\Omega t_{90} \\ \dfrac{\Delta\omega_0^2}{\Omega^2}+\dfrac{\omega_1^2}{\Omega^2}\cos\Omega t_{90} \end{pmatrix}. \qquad [22]$$

It is common practice to use phase cycling to eliminate any offsets in the detection electronics or to eliminate the effects of pulse ringing and magnetoacoustic ringing. The basic phase cycling scheme for the CPMG sequence alternates the phase of the 90° pulse between $-x$ and $+x$ without changing the phase of the 180° pulses. The resulting signal is added and subtracted. We include the effects of phase cycling in the spin dynamics calculation by replacing $\mathcal{R}_{90x}\{\hat{z}\}$ with

$$\mathcal{R}_{\mathcal{A}}\{\hat{z}\} = \frac{1}{2}[\mathcal{R}_{-90x} - \mathcal{R}_{+90x}]\{\hat{z}\} = \frac{\omega_1}{\Omega}\begin{pmatrix} -\dfrac{\Delta\omega_0}{\Omega}(1-\cos\Omega t_{90}) \\ \sin\Omega t_{90} \\ 0 \end{pmatrix}. \qquad [23]$$

Using the fact that $\mathcal{R}_{\mathcal{A}}\{\hat{z}\}$ with phase cycling has only components in the $\hat{x}$–$\hat{y}$ plane and the axis $\hat{n}_{\mathcal{B}}$ has only components in the $\hat{y}$–$\hat{z}$ plane, Eq. [21] simplifies to

$$m_{\infty,y} = n_y^2(\hat{y}\cdot\mathcal{R}_{\mathcal{A}}\{\hat{z}\}). \qquad [24]$$

Using Eqs. [16] for n_y and [23] for $\mathcal{R}_{\mathcal{A}}\{\hat{z}\}$, $m_{\infty,y}$ with phase cycling becomes

$$m_{\infty,y}(\Delta\omega_0,\ \omega_1) = \frac{\omega_1}{\Omega}\frac{\sin(\Omega t_{90})}{1+\left[\dfrac{\Omega}{\omega_1}\sin(\Delta\omega_0 t_E/2)\cot(\Omega t_{180}/2) + \dfrac{\Delta\omega_0}{\omega_1}\cos(\Delta\omega_0 t_E/2)\right]^2}. \qquad [25]$$

The asymptotic normalized magnetization, Eq. [25], is plotted in Fig. 3 as a function of $\Delta\omega_0$ and ω_1. The sweet spot is at $(\Delta\omega_0 = 0,\ \omega_1 = \pi/t_{180})$. At odd multiples of the nominal RF field strength, there are other sweet spots, but the asymptotic magnetization has alternating signs. The additional, bat-like structure depends on the echo spacing, t_E. The stripes are spaced by approximately $\delta\omega_0 = 2\pi/t_E$. Note that if the field inhomogeneity in B_0 is larger than this spacing, the effect of this structure is completely averaged out for echoes within the CPMG. The reason is that the acquisition time for an echo within the CPMG sequence is necessarily less than t_E, leading to a frequency resolution that is coarser than this spacing. The structure can be observed if the field homogeneity is high enough or if the CPMG sequence is stopped and the last echo is acquired with a long acquisition time. The fine structure in the spectrum will then lead to secondary echoes at at times $(n + 1/2)t_E$ after the last refocusing pulse.

4. RELAXATION

4.1. General Expressions

In this section, effects of T_2 and T_1 relaxation during the intervals of free precession between the pulses are analyzed. Relaxation during the RF pulses is neglected.

The following operator describes relaxation during the interval τ_{CP} for the magnetization, normalized to the thermal equilibrium:

$$\mathbb{O}_{\mathcal{R}}\{\mathbf{m}\} = [\Gamma_1(\mathbf{m}\cdot\hat{z}) + (1-\Gamma_1)]\hat{z} + \Gamma_2[\mathbf{m} - (\mathbf{m}\cdot\hat{z})\hat{z}], \qquad [26]$$

where $\Gamma_i \equiv \exp\{-\tau_{CP}/T_i\}$. The expression for the magnetization of the Nth echo, $\mathbf{m}_N$, is modified from a combination of pure rotations in the absence of relaxation, $\mathbf{m}_N = [(\mathcal{R}_{\mathcal{B}})^N\mathcal{R}_{\mathcal{A}}]\{\hat{z}\}$, to an expression involving also the relaxation operator $\mathbb{O}_{\mathcal{R}}$: $\mathbf{m}_N = [(\mathbb{O}_{\mathcal{R}}\mathcal{R}_{\mathcal{B}}\mathbb{O}_{\mathcal{R}})^N\mathcal{R}_{\mathcal{A}}]\{\hat{z}\}$. If we write

$$(\mathbb{O}_{\mathcal{R}}\mathcal{R}_{\mathcal{B}}\mathbb{O}_{\mathcal{R}})\{\mathbf{m}\} \equiv \mathbb{O}_{\mathcal{B}}\{\mathbf{m}\} + \boldsymbol{\rho}, \qquad [27]$$

then the expression for $\mathbf{m}_N$ with relaxation becomes

$$\mathbf{m}_N = [(\mathbb{O}_{\mathcal{B}})^N\mathcal{R}_{\mathcal{A}}]\{\hat{z}\} + \sum_{k=0}^{N-1}(\mathbb{O}_{\mathcal{B}})^k\{\boldsymbol{\rho}\}. \qquad [28]$$

With standard phase cycling, the last term in Eq. [28] does not contribute to the signal. The relevant first term has a form analogous to the expression for the magnetization in the absence of relaxation, Eq. [10]. In the presence of relaxation, the effective rotation $\mathcal{R}_{\mathcal{B}}$ is replaced by the more complicated operator $\mathbb{O}_{\mathcal{B}}$.

It is straightforward to calculate the operator $\mathbb{O}_{\mathcal{B}}$. We list it in the coordinate system spanned by the three vectors $\{\hat{x}; (\Gamma_1/\Gamma_0\ n_z)\hat{y} - (\Gamma_2/\Gamma_0\ n_y)\hat{z};\ (\Gamma_2/\Gamma_0\ n_y)\hat{y} + (\Gamma_1/\Gamma_0\ n_z)\hat{z}\}$, where $\Gamma_0 \equiv \sqrt{\Gamma_1^2 n_z^2 + \Gamma_2^2 n_y^2}$:

$$\mathbb{O}_{\mathcal{B}} = \begin{pmatrix} 0 & 0 & 0 \\ 0 & 0 & 0 \\ 0 & 0 & \Gamma_0^2 \end{pmatrix} + \begin{pmatrix} \Gamma_2^2\cos(\alpha_{\mathcal{B}}) & -\dfrac{\Gamma_1\Gamma_2^2}{\Gamma_0}\sin(\alpha_{\mathcal{B}}) & -\dfrac{\Gamma_2(\Gamma_2^2-\Gamma_1^2)}{\Gamma_0}\, n_y n_z \sin(\alpha_{\mathcal{B}}) \\ \dfrac{\Gamma_1\Gamma_2^2}{\Gamma_0}\sin(\alpha_{\mathcal{B}}) & \dfrac{\Gamma_1^2\Gamma_2^2}{\Gamma_0^2}\cos(\alpha_{\mathcal{B}}) & \dfrac{\Gamma_2\Gamma_1(\Gamma_2^2-\Gamma_1^2)}{\Gamma_0^2}\, n_y n_z \cos(\alpha_{\mathcal{B}}) \\ \dfrac{\Gamma_2(\Gamma_2^2-\Gamma_1^2)}{\Gamma_0}\, n_y n_z \sin(\alpha_{\mathcal{B}}) & \dfrac{\Gamma_2\Gamma_1(\Gamma_2^2-\Gamma_1^2)}{\Gamma_0^2}\, n_y n_z \cos(\alpha_{\mathcal{B}}) & \dfrac{(\Gamma_2^2-\Gamma_1^2)^2}{\Gamma_0^2}\,(n_y n_z)^2\cos(\alpha_{\mathcal{B}}). \end{pmatrix} \quad [29]$$

In general, it is difficult to give the operator $\mathbb{O}_{\mathcal{B}}$ a simple geometrical interpretation. However, there are two important and simple limits: (i) absence of relaxation, $\Gamma_i = 1$. In this case, $\mathbb{O}_{\mathcal{B}}$ reduces to the rotation $\mathcal{R}_{\mathcal{B}}$. (ii) $T_1 = T_2$. In this case, $\Gamma_1 = \Gamma_2 = \Gamma_0 = \exp\{-\tau_{CP}/T_1\}$ and $\mathbb{O}_{\mathcal{B}}$ describes the rotation $\mathcal{R}_{\mathcal{B}}$ followed by an isotropic reduction by $\exp\{-2\tau_{CP}/T_1\}$.

The vector $\boldsymbol{\rho}$ in the same coordinate system as used above for $\mathbb{O}_{\mathcal{B}}$ is given by

$$\boldsymbol{\rho} = (1-\Gamma_1) \times \begin{pmatrix} \Gamma_2\sin(\alpha_{\mathcal{B}})n_y \\ -\dfrac{\Gamma_2}{\Gamma_0}[1+\Gamma_1\cos(\alpha_{\mathcal{B}})]n_y \\ \dfrac{\Gamma_1}{\Gamma_0}[1+\Gamma_1]n_z - \dfrac{\Gamma_1^2-\Gamma_2^2}{\Gamma_0}[1-\cos(\alpha_{\mathcal{B}})]n_y^2 n_z \end{pmatrix}. \quad [30]$$

Using this particular coordinate system, the representation of the operator $\mathbb{O}_{\mathcal{B}}$ in Eq. [29] splits naturally into two parts. The first matrix has only a single nonzero element and it is independent of $\alpha_{\mathcal{B}}$. In contrast, each term in the second matrix is proportional to either $\cos(\alpha_{\mathcal{B}})$ or $\sin(\alpha_{\mathcal{B}})$. To obtain the signal of the Nth echo, the operator has to be raised to the Nth power and then averaged over all the relevant values of $\Delta\omega_0$ and ω_1. The signal will be dominated by the first term, since all the other terms have an oscillatory nature and tend to average out. This is in analogy to the prior argument that the asymptotic signal will be determined by the first term in Eq. [11].

4.2. Signal Offset and Saturation for $T_1 = T_2$

We first treat the case of $T_1 = T_2$. For echo spacings short compared to the relaxation times, $\tau_{CP} \ll T_2$, and after the first few echoes, $t > \tau_{CP}$, we can safely neglect terms that depend on $\alpha_{\mathcal{B}}$. Using Eqs. [28], [29], and [30], we obtain for the normalized magnetization, $\mathbf{m}(t)$,

$$\mathbf{m}(t) \approx (\hat{n}_{\mathcal{B}} \cdot \mathcal{R}_{\mathcal{A}}\{\hat{z}\})\hat{n}_{\mathcal{B}} e^{-t/T_2} + n_z \hat{n}_{\mathcal{B}}(1 - e^{-t/T_2}). \quad [31]$$

The first term is the desired signal. With the assumption $T_1 = T_2$, relaxation simply leads to an exponential decay with the decay time T_2. The second term is an offset term, as has been studied experimentally by Vold *et al.* (*9*). Hughes and Lindblom (*25, 26*) considered the offset term theoretically, but their treatment is restricted to small offset frequencies, $\Delta\omega_0 \ll \omega_1$. The present treatment is valid for all offsets.

The offset term can be separated from the signal term by standard phase cycling. Equation [31] shows that at the end of the CPMG sequence of duration $t \gg T_2$, the baseline offset of the signal is $M_y \to n_y n_z M_0$, and the saturation of the longitudinal magnetization is $M_z \to n_z^2 M_0$. As expected, $M_z \to 0$ on resonance and $M_z \to M_0$ far off resonance. Note that the magnetization at long time is independent of relaxation time. In inhomogeneous fields, the offset of the signal at the nominal echo center tends to be small, because $n_y n_z$ is a rapidly oscillating function with respect to $\Delta\omega_0$. However, this term describes the "steady-state-free-precession" signal (*27, 28*) in inhomogeneous fields that can be observed before and after the nominal 180° RF pulses.

4.3. Observed Relaxation Time for $T_1 \neq T_2$

When $T_1 \neq T_2$, the situation is more complicated. We assume standard phase cycling and only consider the signal term that is independent of $\alpha_{\mathcal{B}}$. The decay of the transverse magnetization depends both on T_1 and on T_2. Relaxation adds a nontrivial decay term to the expression for the asymptotic normalized magnetization:

$$m_N \approx \{n_y^2 e^{-2\tau_{CP}/T_2} + n_z^2 e^{-2\tau_{CP}/T_1}\}^N n_y^2(\hat{y} \cdot \mathcal{R}_{\mathcal{A}}\{\hat{z}\}). \quad [32]$$

In general, the signal decay is not single exponential anymore, but decays with a distribution of decay times between T_1 and T_2. The initial decay rate of Eq. [32] is given by the simple expression

$$\frac{1}{T_{2,\text{eff}}} = \langle n_y^2 \rangle \frac{1}{T_2} + \langle n_z^2 \rangle \frac{1}{T_1} = \frac{1}{T_2} - \langle n_z^2 \rangle \left(\frac{1}{T_2} - \frac{1}{T_1} \right). \quad [33]$$

Here $0 \leq \langle n_z^2 \rangle \leq 1$ is the average of the square of the projection of the effective axis $\hat{n}_{\mathcal{B}}$ onto the z-axis. The effective decay rate is a weighted sum of the T_1 and T_2 relaxation rates, with weights determined by the direction of the effective axis $\hat{n}_{\mathcal{B}}$. Note that this expression for the initial decay rate has the same form as the effective relaxation rate in spin-lock experiments under off resonant conditions (*29*). In that case, T_2 in Eq. [33] is replaced by $T_{1\rho}$ and n_z is replaced by the z-component of the axis of the effective RF field, $\Delta\omega_0/\Omega$. For the CPMG sequence, the relevant axis is not that of the effective RF field, but the axis $\hat{n}_{\mathcal{B}}$ that describes the whole refocusing cycle, including the free precession between the pulses.

The total signal displays an initial transient associated with the magnetization perpendicular to the effective axis $\hat{n}_{\mathcal{B}}$. Afterward, the signal is dominated by the magnetization "spin-locked" to $\hat{n}_{\mathcal{B}}$ and decays with the initial rate $1/T_{2,\text{eff}}$. An explicit example is shown in Section 5.5.

For a given field map, $\langle n_z^2 \rangle$ is a constant independent of relaxation times. The average of n_z^2 is calculated by weighting it with the expected signal in the absence of relaxation, Eqs. [12, 24],

$$\langle n_z^2 \rangle = \frac{\begin{array}{r}\iint d\Delta\omega_0 d\omega_1 f(\Delta\omega_0, \omega_1)(\omega_{\text{RF}} - \Delta\omega_0)^2 \\ \times F(\Delta\omega_0) m_{\infty,y}(\Delta\omega_0, \omega_1) n_z^2(\Delta\omega_0, \omega_1)\end{array}}{\begin{array}{r}\iint d\Delta\omega_0 d\omega_1 f(\Delta\omega_0, \omega_1)(\omega_{\text{RF}} - \Delta\omega_0)^2 \\ \times F(\Delta\omega_0) m_{\infty,y}(\Delta\omega_0, \omega_1)\end{array}}. \quad [34]$$

Bull (*10*) has previously calculated the effective decay rate for the specific case of $\Delta\omega_0 = -\pi/t_E$. His result, (Eq. [40] in (*10*)), is in agreement with the more general result in Eq. [33]. Goelman and Prammer (*13*) have presented numerical results for the effective relaxation time $T_{2,\text{eff}}$ as a function of the ratio of T_1/T_2 for another NMR logging device. We show in Section 5.5 that their numerical results are well described by Eq. [33].

Relaxation during the RF pulses has been neglected. When short echo spacings are used, the treatment has to be expanded to include $T_{1,\rho}$ relaxation effects.

5. APPLICATION TO THE NMR LOGGING TOOL

In this section, we apply the spin dynamics calculations to characterize an "inside-out" NMR apparatus used for oil-well logging (*1*). Such instruments are used for *in situ* evaluation of geological formations in boreholes up to 10 km deep and temperatures up to 175°C. This NMR apparatus has been described in detail by Kleinberg *et al.* (*17*). The magnetic field is generated by two SmCo magnets, magnetized transverse to the sonde axis and arranged in a way to create a sweet spot in the formation. At the sweet spot, the field forms a saddle point with the magnetic field pointing predominantly in the radial direction. The RF field is generated by a 15-cm-long half coaxial cable placed on the face of the sonde (*30*). At the saddle point, the RF field is transverse to the static field. The face of the RF sensor is pressed against the wall of the borehole. Under normal operation, the whole NMR apparatus is pulled upward and the NMR response of the earth formations is continuously measured using the CPMG sequence.

5.1. Field Maps

In order to calculate the signal strength at any given point in space, both the magnitude and the direction of the static and RF field have to be known. We mapped the vectors of the static field, $\mathbf{B}_0(\mathbf{r})$, and the RF field normalized by the square root of RF power, $\mathbf{B}_1(\mathbf{r})/\sqrt{P}$, in all three dimensions. Details are discussed in the Appendix. From these field maps, maps of the detuning frequency $\Delta\omega_0$ and the RF strength ω_1 are generated. Figure 4 shows the $|\Delta\omega_0|$ and ω_1 maps in a cross section perpendicular to the sonde axis at the position halfway along the RF sensor. The radial direction x is measured outward from the outer most face of the NMR apparatus; the tangential direction y is centered at the symmetry plane of the tool.

With this magnet arrangement, the sweet spot is located slightly over an inch into the formation. At the sweet spot, the field strength is 541.2 G, corresponding to a Larmor frequency of 2.3 MHz. The magnetic field strength is decreasing radially away from the saddle point and increasing in the transverse direction closer to the pole pieces of the two magnets. The strength of the RF field $|\mathbf{B}_1(\mathbf{r})|$ increases monotonically toward the RF sensor. However, for NMR applications, only the component of the RF field perpendicular to the static field contributes to ω_1. In the transverse plane, ω_1 vanishes along two lines where the fields $B_0(\mathbf{r})$ and $B_1(\mathbf{r})$ are parallel.

Using the field maps shown in Fig. 4, the sensitivity map is calculated and displayed in Fig. 5 for the same cross section as before. The sensitivity is the integrand of Eq. [5], using the asymptotic magnetization of Eq. [24]. There are no significant regions with negative sensitivity. Ideally, a matched filter is used for $F(\Delta\omega_0)$ in Eq. [5]. For the purpose of this calculation, we have used a simple filter of the form $F(\Delta\omega_0) = \text{sinc}^2(\Delta\omega_0 T_{\text{filter}}/4)$, with $T_{\text{filter}} = 2t_{180}$.

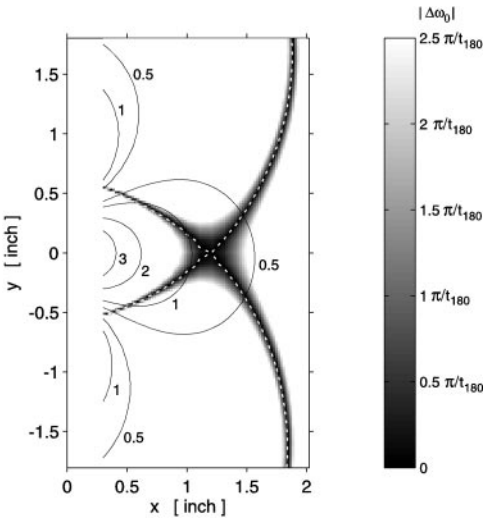

FIG. 4. Map of the measured static and RF fields in a cross section through the plane perpendicular to the sonde axis at the position halfway along the RF sensor. The grayscale image displays $|\Delta\omega_0|$. For the value of $t_{180} = 29.2\ \mu s$, $\Delta\omega_0 = \pi/t_{180}$ corresponds to a field variation of 4 G from the field strength of 541.2 G at the sweet spot. Exact resonance, $\Delta\omega_0 = 0$, is shown by the dotted line. To the left and right of the sweet spot, the strength of the static field B_0 decreases and $\Delta\omega_0 > 0$, whereas to the top and bottom of the sweet spot, $\Delta\omega_0 < 0$. The solid lines are contours of constant values of ω_1. The curves are labeled by $\omega_1 t_{180}/\pi$, i.e., the ratio of the local RF field to the ideal value.

The sensitivity map in Fig. 5 has a similar shape as the $\Delta\omega_0$ map in Fig. 4. The signal is dominated by contributions coming from the region around the sweet spot and from the two "spider legs" extending toward the RF sensor. The other two spider legs are attenuated, because the RF field decreases rapidly in the radial direction.

Also shown in Fig. 5 are contour lines of constant gradient, $|\nabla \mathbf{B}_0|$. Close to the sweet spot they form circles, characteristic for a saddle point. The effect of these gradients will be further discussed in Section 6.

5.2. Distribution Function of $\Delta\omega_0$ and ω_1

For the calculation of the total NMR signal, we have to integrate the sensitivity over three dimensions. As pointed out above, the integral can be reduced to a two-dimensional integral over $\Delta\omega_0$, ω_1 by calculating the distribution function $f(\Delta\omega_0, \omega_1)$, defined in Eq. [6]. Figure 6 shows the distribution function for the current NMR apparatus extracted from the measured field maps.

This distribution function is peaked near the sweet spot $(\Delta\omega_0, \omega_1) = (0, \pi/t_{180})$, but has significant contributions away from it. It is intermediate between two extreme cases. For a homogeneous field, the distribution function would be a delta-function centered at the sweet spot. In a gradient field, such as encountered in stray field NMR (*4*) or in logging tools with fields approximated by two-dimensional dipoles (*13*), the distribution function $f(\Delta\omega_0, \omega_1)$ has only contributions on a nearly horizontal line going through the sweet spot $(\Delta\omega_0, \omega_1) = (0, \pi/t_{180})$ with a slope of $\nabla B_1/\nabla B_0 \ll 1$.

5.3. Transient Behavior of the First Few Echoes

The amplitudes of the first few echoes show a distinct transient behavior. In Fig. 7, the calculated amplitudes of the first 15 echoes are compared with CPMG measurements performed with the logging tool, using a large bottle of water as a sample. Both in-phase and out-of-phase amplitudes are shown. There is excellent agreement between measurements and calculations. For the solid line, the signal (Eq. [6]) was calculated using the full expression for the magnetization, $\mathbf{m}_N$, Eq. [11]. It is normalized with respect to the asymptotic signal, Eq. [12].

The data in Fig. 7 show that the second and third terms in $\mathbf{m}_N$, Eq. [11], are only relevant for the first two echoes. For a higher echo number, the integration over the field distribution averages these terms to zero to a high degree. This demonstrates that the expression for the asymptotic signal, Eq. [12], is an excellent approximation for the observed signal. The out-of-phase component is less than 1% of the asymptotic in-phase value for all echo numbers. Therefore, the transient spin dynamics effect does not affect the determination of the proper signal phase. The transient behavior for the first two echoes shows a negligible dependence on t_E for $t_E \leq 1$ ms. At longer echo spacings, diffusion effects become important. This is further discussed in Section 6. For weaker field inhomogeneities, the transient effect is smaller on the first two echoes but extends over a larger number of echoes.

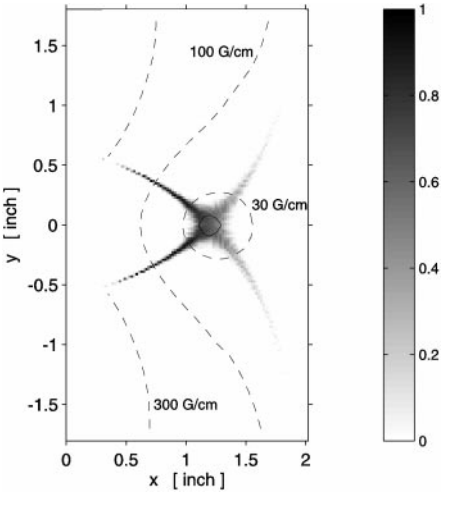

FIG. 5. Sensitivity map in the cross section through the plane perpendicular to the sonde axis at the position halfway along the RF sensor. The grayscale is proportional to the signal generated by spins located at that point. The dashed lines are contour lines of constant gradient for 30, 100, and 300 G/cm, respectively. The solid line indicates the 10 G/cm contour.

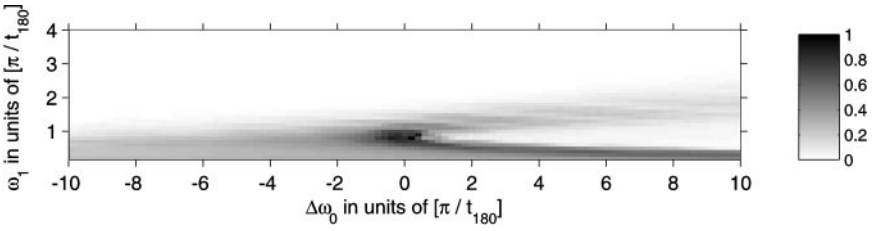

FIG. 6. Distribution function $f(\Delta\omega_0, \omega_1)$ for the field map of the logging tool, normalized to a maximum of 1. The distribution function is defined such that $f(\Delta\omega_0, \omega_1)\ \delta\Delta\omega_0\ \delta\omega_1$ is proportional to the volume of spins with $\Delta\omega_0 \pm \delta\Delta\omega_0$ and $\omega_1 \pm \delta\omega_1$, multiplied by the coil efficiency factor ω_1/I.

5.4. Phase

For the CPMG sequence, the axis describing the refocusing cycle, $\hat{n}_{\mathcal{B}}$, is in the $\hat{y}$–$\hat{z}$ plane for all values of $\Delta\omega_0$ and ω_1. As stated above, this implies that the phase of the asymptotic signal is along the $\hat{y}$ direction, independent of the exact nature of the inhomogeneities. This has been tested by detuning the logging tool from the sweet spot of the saddle point. Using two large coils, an external magnetic field was applied to the logging tool roughly parallel to the field produced by the permanent magnets. This external field was varied between -18.8 and $+18.8$ G, corresponding to a change in Larmor frequency of ± 80 kHz. This is significantly larger than the typical strength of the RF field, which is of order $\omega_1/2\pi \simeq 1/2t_{180} = 17.1$ kHz.

CPMG measurements were taken as a function of the applied field. The RF frequency and all other acquisition parameters were kept constant. An applied field of ± 18.8 G shifts the distribution function $f(\Delta\omega_0, \omega_1)$ shown in Fig. 6 along the $\Delta\omega_0$ axis by $\delta\omega_0 = \pm 4.7\pi/t_{180}$. In this case, the signal originates not from the sweet spot at the saddle point anymore, but from two thin crescents. The associated resonant volume is reduced, which leads to a decrease in signal amplitude by over a factor of 2.

Detuning from the sweet spot does not affect the phase of the signal significantly, as is shown in Fig. 8. This supports the previous conclusion from Fig. 7 that the signal is dominated by the magnetization spin-locked to the axis $\hat{n}_{\mathcal{B}}$. This behavior, independent on the exact field profile, is contrasted in Fig. 8 with the phase of a free induction decay in a homogeneous field where detuning leads to a rapid phase change.

5.5. Relaxation

In Section 4, the theory of relaxation in the presence of inhomogeneous fields for the CPMG sequence was developed. It was shown that for $T_1 \neq T_2$, the overall decay of the detected transverse magnetization is not single exponential anymore and that the initial decay rate is a weighted sum of T_2^{-1} and T_1^{-1}.

In Fig. 9, calculations for the field maps of the present NMR logging tool are presented. The solid line shows the result of solving the full spin dynamics problem, Eq. [28], numerically for the field maps of the NMR logging tool using the relaxation parameters $T_2 = 30$ ms and $T_1 = 90$ ms. The echo spacing was set to $t_E = 1$ ms and standard phase cycling was used. We

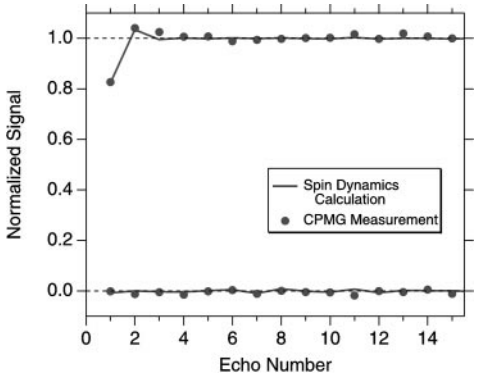

FIG. 7. Transient behavior of the first 15 in-phase (top) and out-of-phase (bottom) echo amplitudes. The solid lines are the calculated echo amplitudes based on the measured field maps using the full expression for the spin dynamics. The dots show the results of CPMG measurements with a water sample and using an echo spacing of $t_E = 320\ \mu$s. The data are normalized with respect to the asymptotic limit of the in-phase signal. Only the in-phase amplitudes of the first two echoes show a significant deviation from the asymptotic limits, shown as dashed lines.

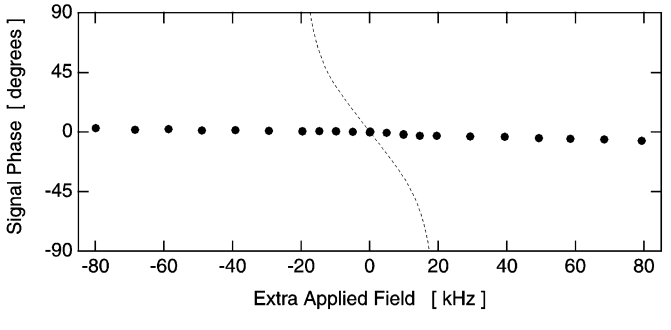

FIG. 8. The change of the measured phase of the NMR signal is plotted versus the additional field, $\gamma B_{app}/2\pi$, applied to the logging apparatus. The RF frequency, coil tuning, and pulse sequence were kept unchanged. The phase shows only a weak dependence on the applied field, indicating that the magnetization contributing to the signal is effectively "spin-locked" to the axis $\hat{n}_{\mathcal{B}}$. In contrast, the calculated phase change of the free induction decay in a homogeneous field with the same nominal RF field strength depends strongly on detuning, as shown by the dashed line.

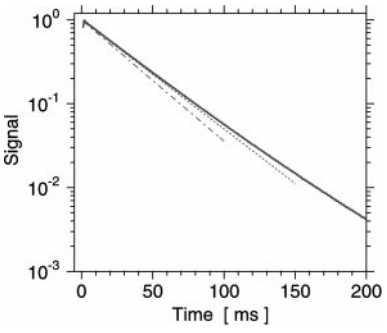

FIG. 9. Relaxation: The solid line is an exact spin dynamics calculation using the measured field maps and assuming $T_2 = 30$ ms and $T_1 = 90$ ms. The initial decay rate is slower than T_2^{-1} (dash–dotted line) but agrees with $1/T_2 - \langle n_z^2 \rangle (1/T_2 - 1/T_1) = (33.4 \text{ ms})^{-1}$ (dashed line). At longer times, the decay deviates from a single exponential.

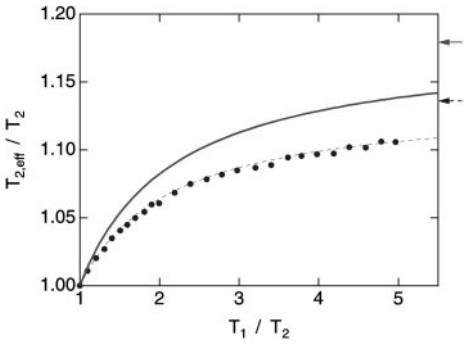

FIG. 10. Ratio of the CPMG relaxation time measured with the logging tool, $T_{2,\text{eff}}/T_2$, as a function of the ratio of T_1/T_2. The solid line is the result of the spin dynamics calculations for the device described here. For our device, $\langle n_z^2 \rangle = 0.15$. The dots show numerical simulations published by Goelman and Prammer (*13*) for a different NMR logging device. The dashed line is a fit to those simulations with $\langle n_z^2 \rangle = 0.12$. Arrows indicate the limiting values of $T_{2,\text{eff}}/T_2$ for $T_1 \gg T_2$ for the two cases.

assume that the spins are initially in thermal equilibrium and that diffusion is negligible. Relaxation during the pulse is neglected. The time axis in Fig. 9 only includes the time of free precession.

The amplitudes of the first and second echoes show the characteristic transient behavior. The deviation of these echoes from the smooth extrapolation from the later echoes agrees with the previous results in Section 5.3 obtained without relaxation. After the second echo, the signal decays in a smooth manner. The decay rate is clearly slower than $1/T_2$, shown by the dashed–dotted line. The theoretical expression for the initial decay rate, Eq. [33], is shown by the dashed line. For our field maps, the value of $\langle n_z^2 \rangle$ has been evaluated numerically to be 0.15. There is excellent agreement between the simple theoretical expression and the simulations. At lower signal levels, the decay starts to deviate from the exponential decay. This is also in agreement with our predictions: The initial decay rate of $1/T_2 - \langle n_z^2 \rangle (1/T_2 - 1/T_1)$ slows down to the limiting rate of $1/T_1$.

For the current NMR device, the measured initial decay rates will vary between T_2 for $T_1 = T_2$ and the limiting case of $T_2/\langle n_y^2 \rangle = 1.17 T_2$ for $T_1 \gg T_2$. This is shown in Fig. 10, where $T_{2,\text{eff}}/T_2$ is plotted as a function of the ratio of T_1/T_2, following Eq. [33].

In Fig. 10, we have also included results for a different NMR logging tool published by Goelman and Prammer (*13*). They used numerical simulations to obtain $T_{2,\text{eff}}/T_2$ as a function of T_1/T_2. This NMR apparatus has a very different field map compared to our device, but their simulation results can still be well described by Eq. [33]. The field maps are described to first order by two-dimensional dipoles. For such field maps, the parameter $\langle n_z^2 \rangle$ is calculated to be 0.09. The fit shown in Fig. 10 to the numerical data gives $\langle n_z^2 \rangle = 0.12$. The difference gives an indication of the end effects where the fields deviate from pure two-dimensional dipole fields.

6. DIFFUSION

For samples with intrinsically long relaxation times, the decay of the observed CPMG echo trains is often controlled by diffusion in field inhomogeneities. In our apparatus, the magnetic field is relatively uniform near the saddle point. Moving away from the saddle point, the gradient $g \equiv |\nabla (|\mathbf{B}_0|)|$ increases to first order linearly. Figure 5 shows that the local gradient strength in the sensitive region of our apparatus varies over a wide range. Close to the saddle point, the gradient strength is less than 10 G/cm, but significant signal comes from regions with gradient strength in excess of 100 G/cm.

The effect of diffusion in these gradients is clearly evident in Fig. 11. A large bottle of water was placed on the apparatus and the decay of the echo amplitudes measured for six different echo spacings, $t_E = 0.32$, 0.65, 1, 2, 5, and 10 ms, respectively. The strong dependence of the decay rate on echo spacing is a clear indication of diffusion effects.

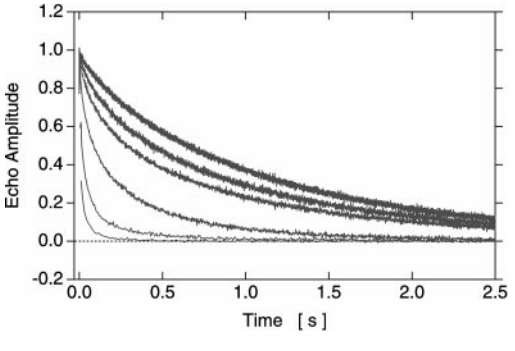

FIG. 11. CPMG measurements with different echo spacings show the effect of diffusion in the inhomogeneous field of the inside-out NMR device. The sample was a big bottle of water placed on the logging tool. The values of echo spacings are $t_E = 0.32$, 0.65, 1, 2, 5, and 10 ms, respectively, increasing from the top curve to the bottom curve.

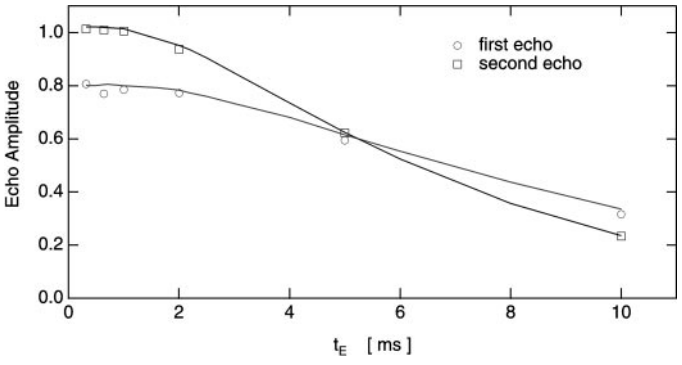

FIG. 12. Amplitude of the first and second echoes as a function of echo spacing. The symbols show measured values; the solid lines show the result of calculations based on the measured field maps that take diffusion in the local gradient into account. The sample is a large bottle of water at room temperature.

With diffusion, spins experience time-dependent refocusing cycles. The axis $\hat{n}_{\mathcal{B}}$ starts to fluctuate and subsequent rotations do not commute anymore. To describe the effect of diffusion quantitatively, we first consider that spins diffuse only over a distance between a few micrometers and a few tens of micrometers before they dephase. Over this length scale, the inhomogeneities in the B_0 field of the apparatus can be well approximated by local gradients; curvature terms are not important. Over these distances, the direction of the static field $\mathbf{B}_0$ changes only by a small amount so that the spins can follow adiabatically. Therefore, it is the gradient of magnitude in B_0, $g = |\nabla|\mathbf{B}_0||$, that determines the dephasing for diffusion. In our case, B_1 gradients can be neglected to a good approximation.

6.1. Diffusion Effect on the First Two Echoes

Woessner (*31*) has studied the effect of diffusion in inhomogeneous fields for up to four pulses. His calculation keeps track of the extra phase shifts that the transverse magnetization acquire between pulses due to the fluctuating magnetic field the spins experience. The resulting attenuation is obtained after integrating over the distribution of the phase shifts, taking into account the appropriate correlations for unrestricted diffusion. We have used the treatment of Woessner to model the observed effect of diffusion on the first two echoes in Fig. 11.

We have generalized the calculation in (*31*) by including effects of RF pulses far off resonance, i.e., take into account that the RF pulses rotate around an axis with a significant $\hat{z}$ component. The expressions derived for this case are summarized in Appendix B. Some of the terms have already been obtained by Goelman and Prammer (*13*). At every point in the sensitive region, the local gradient was determined from the measured field maps and the echo amplitude for the first two echoes was calculated as a function of echo spacing using Eqs. [39] to [48]. The diffusion coefficient was set to $D_0 = 2.3 \times 10^{-5}$ cm^2/s, appropriate for water at room temperature. The results for the calculated echo amplitudes, integrated over all space, are shown in Fig. 12 and compared with the measurements from Fig. 11.

There is excellent agreement between calculation and measurements. For short echo spacings, the behavior of the first two echo amplitudes is determined primarily by the spin dynamics interplay between the first term in Eq. [11] and the other two terms. As was discussed in Section 5.3, the second and third terms overall subtract from the first term for the first echo, but add for the second echo. This leads to the characteristic transient behavior with a decreased first echo amplitude, shown in Fig. 7.

With larger echo spacings, diffusion modifies this transient behavior of the first two echoes. Diffusion attenuates the second echo more than the first echo. As a results, there is a crossover at echo spacings of around 5 ms, when the amplitude of the second echo drops below the amplitude of the first echo.

6.2. Gradient Distribution

For a larger number of echoes, this approach for calculating the effect of diffusion of the CPMG sequence in grossly inhomogeneous fields becomes unmanageable, because the number of coherences that must be considered diverges.

In our application, there is a large range of local gradients. In Fig. 13, the solid line shows the gradient distribution $f(g)$ calculated from the measured field maps. At every point in space, the local gradient is calculated and it contributes to $f(g)$ according to the local asymptotic sensitivity, i.e., the integrand of V_∞ (Eq. [5]) using the asymptotic magnetization $m_{\infty,y}$ (Eq. [24]). In Fig. 13, the gradient distribution is displayed as a function of $\log(g)$ and is normalized so that $\int d \log g\, f(\log g) = 1$. The distribution has a maximum at around 20 G/cm but with significant contributions over a range of almost two orders of magnitude in gradient strength.

For weak inhomogeneities, it is well known (*7, 32*) that diffusion in a gradient g leads to an extra attenuation of $\exp\{-\frac{1}{12}\gamma^2 g^2 D_0 t_E^2 t\}$. This corresponds to the case when $n_z = 0$. Kaiser *et al.* (*33*) have analyzed the effect of diffusion in

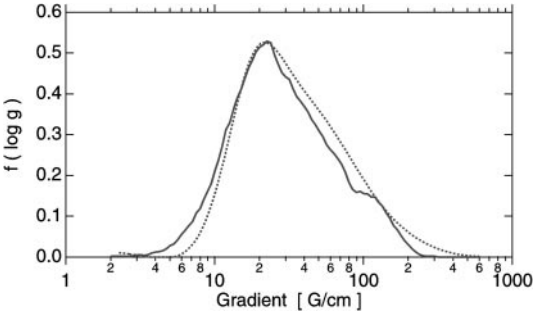

FIG. 13. Gradient distribution for logging tool: The solid line shows the distribution derived from the measured field maps. The dotted line shows the gradient distribution deduced from the CPMG measurements, assuming a value of the efficiency factor $\eta = 1$.

inhomogeneous fields when a large number of identical RF pulses are applied. They found that when the signal has contributions from many different coherences (in our language $n_z \neq 0$), the signal decay due to diffusion is faster than for the on-resonance case. They introduced the efficiency factor $\eta > 1$ to measure the increase in decay rate. For our case, we approximate the signal decay for the CPMG sequence in inhomogeneous fields, after the first few echoes, by

$$M(t) \approx M_0 \exp\left\{-\frac{t}{T_2}\right\} \int dg f(g) \times \exp\left\{-\frac{1}{12}\eta\gamma^2 g^2 D_0 t_E^2 t\right\}. \quad [35]$$

In principle, the efficiency factor η has a complicated dependence on $\Delta\omega_0$, ω_1, and the pulse parameters. However, we find that within experimental error, the diffusion-related signal decay in Fig. 11 scales like $t_E^2 t$. This indicates that, for our analysis, we can ignore the dependence of η on other parameters and replace it to first order by a constant.

We have used Eq. [35] to extract independently a distribution of gradients, $f(g)$, from the measured signal decay after the first few echoes. The fitting routine used was originally developed by Sezginer for relaxation time distributions (*34*). The bulk relaxation time of water was independently measured in a standard NMR set up with homogeneous field at 2 MHz. For this analysis, we set the efficiency parameter $\eta = 1$. The diffusion coefficient was set to $D_0 = 2.3 \times 10^{-5}$ cm^2/s. The resulting gradient distribution is shown as a dotted line in Fig. 13.

The two gradient distributions, shown in Fig. 13, show a remarkable agreement, considering that they were obtained in completely independent ways. Closer inspection shows that the measurement derived distribution appears to be shifted slightly to the right by about 15% compared with the field-map-based distribution. This can be interpreted that the efficiency factor η is not 1 as assumed in the data analysis, but is $\langle\eta\rangle \approx 1.3$.

To use this measurement for the extraction of fluid diffusion coefficients in real formations, two complications arise. First, susceptibility contrasts between the rock grain and the pore filling fluids lead to induced gradients that can be comparable to these tool gradients (*35*). Second, in the pore space of the rock, diffusion of the spins is restricted and not free as assumed above. If the pore size is smaller than the dephasing length $l_g \equiv (D_0/(\gamma g))^{1/3}$, the effects of restrictions are important (*36*). Typical values of l_g are in the range of a few to 10 μm, comparable to the pore size in many formations.

7. CONCLUSIONS

We have shown that the spin dynamics of the CPMG in grossly inhomogeneous fields can be analyzed effectively by considering the axis, $\hat{n}_{\mathcal{B}}$, that characterizes the refocusing subcycle from one echo to the next. This is essentially the eigenvector of the propagator of the refocusing subcycle associated with the eigenvalue 1. After the first few echoes, the signal is dominated by the magnetization spin-locked to this eigenvector. The components of the magnetization after the initial 90° pulse that fall onto the other two eigenvectors give rise to a transient behavior of the first few echo amplitudes, but then average out to a high degree. For the CPMG sequence, in the absence of diffusion or motion effects, the axis $n_{\mathcal{B}}$ is always in the y–z plane in the rotating frame. As a consequence, the phase of the echoes is independent of the exact field distribution. These results have been confirmed with experiments on a inside-out NMR logging tool with very inhomogeneous fields.

When the axis $n_{\mathcal{B}}$ has a significant z-component, the signal has an offset at long times. It can be eliminated by phase cycling. In addition, when $T_1 \neq T_2$, it gives rise to a nonexponential signal decay with an initial decay rate that is a weighted sum of T_1 and T_2 relaxation rates.

This approach is also useful for the analysis of effects due to motion, instabilities of pulse parameters, or diffusion.

APPENDIX A

Field Maps

A.1. Measurement of Field Maps

Each component of the static field $\mathbf{B}_0(\mathbf{r})$ was mapped using a one-axis Hall probe [F. W. Bell, Inc., Digital Gaussmeter, Model 811AB and SAK 8-1808 probe]. The probe was mounted to a three-axis computer-directed positioner that scanned the field in front of the magnets. The probe was then reoriented and the next component of $\mathbf{B}_0(\mathbf{r})$ was measured.

For the measurement of the normalized RF field, $\mathbf{B}_1(\mathbf{r})/\sqrt{P}$, a HP3577A network analyzer was used. The RF sensor was driven at its resonant frequency, ω_c. A pick-up loop, mounted to the same three-axis computer-directed positioner, scanned sequentially the three components of the RF field in front of the antenna. The voltage induced in the single turn, 0.202-inch diameter, pick-up loop drove the balanced terminals of a 50-ohm 1:1 balanced to unbalanced transformer. The normalized zero-to-peak RF field along the axis of the pick-up loop was determined from the measured S-parameters S_{ij} by

$$\frac{B_1}{\sqrt{P}} = S_{21} \frac{2}{(1 - S_{22}) N_t A \omega_c} \sqrt{\frac{2Z_0}{1 - |S_{11}|^2}}. \quad [36]$$

Here P is the power dissipated in the antenna and its tuning capacitors, $N_t = 1$ is the number of turns on the pick-up loop, $A = 2.07 \times 10^{-5}$ m^2 is the area of the pick-up loop, and $Z_0 = 50\ \Omega$ is the input/output impedance of the network analyzer.

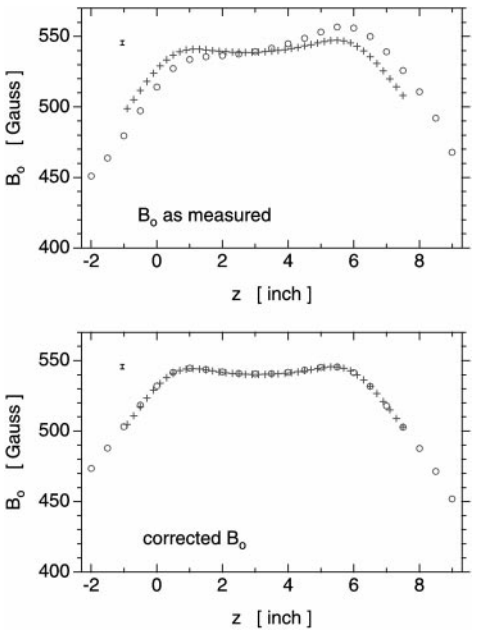

FIG. 14. Profiles of $|\mathbf{B}_0|$ from two different field scans through the sweet spot along the axis of the NMR apparatus. (Top) Data as measured. There is a large discrepancy between the two measurements, caused by a small misalignment of the Hall probe for the separate measurements of the three field components. (Bottom) Corrected data. For each measurements, the angles describing the probe misalignments were determined separately by minimizing $|\nabla \times \mathbf{B}_0|^2$. There is excellent agreement between the two corrected field measurements. The small error bar on the upper left shows a typical value of B_1.

A.2. Corrections to the Field Maps

For our application, the accuracy of the B_0 measurement has to be much better than the local value of B_1, i.e., much better than 1%. In Fig. 14A, two independently measured profiles of the magnitude $|\mathbf{B}_0(\mathbf{r})|$ are shown on a line through the sweet spot along the axis of the NMR sensor. Instead of a perfect overlay, the two curves deviate from each other by as much as 10 G, an amount much larger than the typical value of B_1.

This deviation is caused by the imperfect reorientation of the Hall sensor that is necessary between measurements of the three field components. As a consequence, when the probe is nominally reoriented by 90° to measure the next field component, the sensor does not measure a component that is exactly orthogonal to the previous measurement. A systematic correction of the data for this tilt is required. This tilt has two independent contributions. First, according to the manufacturer's specifications, there is an uncertainty in the orientation of the chip sensing the Hall voltage of ±2°. Second, we estimate that our alignment of the probe is accurate to about the same level, ±2°.

Two angles are required to describe the actual orientation of the Hall sensor relative to the nominal direction. For all three components, this results in a total of six angles that have to be determined. For a given data set, the measured fields, $\mathbf{B}_{0,m}$, are related to the true fields, $\mathbf{B}_0$, by

$$\mathbf{B}_{0,m} = \begin{pmatrix} \sqrt{1-\varepsilon_{x,y}^2-\varepsilon_{x,z}^2} & \varepsilon_{x,y} & \varepsilon_{x,z} \\ \varepsilon_{y,x} & \sqrt{1-\varepsilon_{y,x}^2-\varepsilon_{y,z}^2} & \varepsilon_{y,z} \\ \varepsilon_{z,x} & \varepsilon_{z,y} & \sqrt{1-\varepsilon_{z,x}^2-\varepsilon_{z,y}^2} \end{pmatrix} \times \mathbf{B}_0. \quad [37]$$

Here $\varepsilon_{i,j} = \sin\theta_{i,j}$ with $i, j = x, y$, or z and where $\theta_{i,j}$ is the angle between the true $\hat{\imath}$ axis and the projection of the actual orientation of the Hall probe onto the $(\hat{\imath}, \hat{\jmath})$ plane.

Maxwell's equations require that the curl of any static magnetic field vanishes (*37*):

$$\nabla \times \mathbf{B}_0 = 0. \quad [38]$$

We estimated $\nabla \times \mathbf{B}_{0,m}$ from the discrete points of the measured field map and found systematically nonzero values, caused by the misalignment of the Hall probe. This allows us to determine the angles $\theta_{i,j}$ in a robust way by minimizing the square of the estimated curl of $\mathbf{B}_0$, $|\nabla \times \mathbf{B}_0|^2$. We observe fast convergence with the solutions $(\theta_{x,y}, \theta_{x,z}, \theta_{y,x}, \theta_{y,z}, \theta_{z,x}, \theta_{z,y}) = (3.3°, -0.6°, 2.3°, 2.4°, 1.9°, -3.0°)$ for the fine scale map and (1.9°, 3.4°, 1.8°, 2.3°, 2.1°, −3.8°) for the large scale map, respectively. These angles are within our estimated accuracy of orienting the Hall probe. The residual of $\langle|\nabla \times \mathbf{B}_0|^2\rangle$ is typically over 100 times smaller for the corrected field maps than for the uncorrected maps.

Figure 14B compares the field profiles of the two independently corrected field maps. The corrected field maps are now in excellent agreement. For all spin dynamics calculations of the NMR logging tool, only the corrected field maps were used.

APPENDIX B

Spin Dynamics of the First Two Echoes with Diffusion

In this Appendix, the general expressions for the first two echo amplitudes with diffusion and for arbitrary offset frequency $\Delta\omega_0$ and RF field strength ω_1 are summarized. Details of the calculation will be given elsewhere. Diffusive attenuation is caused by the extra random phases the spins acquire between the pulses because the spins diffuse into regions with different Larmor frequency. Following Woessner (*31*), the evolution for every different possible diffusion path is first calculated. The final result is obtained after averaging over all possible paths. Unrestricted diffusion in a gradient of strength g and standard two-step phase cycling are assumed.

The effect of diffusion on the RF pulses is neglected, i.e., it is assumed that the RF strength ω_1 and the offset frequency

$\Delta\omega_0$ is time independent for all of the RF pulses. This is appropriate in our case, since the gradient of B_1 is much smaller than the gradient in B_0 and the duration of the pulses is much shorter than the echo spacing.

The y-magnetization, normalized to the thermal magnetization M_0, at the time of the first echo, is given by

$$m_{1,y} = a_1 \exp\left\{ -\frac{2}{3}\gamma^2 g^2 D_0 \tau_{cp}^3 \right\} + a_2 \exp\left\{ -\frac{8}{3}\gamma^2 g^2 D_0 \tau_{cp}^3 \right\}, \quad [39]$$

with

$$a_1 = \left(\frac{\omega_1}{\Omega}\right)^3 \sin(\Omega t_{90}) \sin^2(\Omega t_{180}/2) \quad [40]$$

$$a_2 = \frac{\omega_1}{\Omega}\sin(\Omega t_{90})\left[\frac{\omega_1}{\Omega}\sin^2(\Omega t_{180}/2) + \cos\alpha_{\mathcal{B}}\right] - \frac{\omega_1}{\Omega}\frac{\Delta\omega_0}{\Omega}[1-\cos(\Omega t_{90})] n_z \sin\alpha_{\mathcal{B}}. \quad [41]$$

The quantities n_y, n_z, and $\alpha_{\mathcal{B}}$ have been defined by Eqs. [16–18]. The second term in Eq. [39] comes from the part of the free induction decay of the first pulse that does not get refocused by the second pulse. Terms due to the free induction decay of the second pulse do not appear, because they have been eliminated by phase cycling.

For the second echo, the y-magnetization, normalized to the thermal magnetization M_0, is the sum of six terms:

$$m_{2,y} = \sum_{i=1}^{6} b_i \exp\{-\eta_i \gamma^2 g^2 D_0 \tau_{cp}^3\}. \quad [42]$$

The parameters $\eta_1, \eta_2 \ldots \eta_6$ are 4/3, 8/3, 10/3, 14/3, 46/3, and 64/3 and the coefficients b_i are given by

$$b_1 = \left(\frac{\omega_1}{\Omega}\right)^5 \sin(\Omega t_{90}) \sin^4(\Omega t_{180}/2) \quad [43]$$

$$b_2 = \frac{1}{2}\left(\frac{\omega_1}{\Omega}\right)^3 \sin(\Omega t_{90})\left[\sin^2(\Omega t_{180}) + \left(\frac{\Delta\omega_0}{\Omega}\right)^2 [1-\cos(\Omega t_{180})]^2\right] \quad [44]$$

$$b_3 = \frac{1}{4}\frac{\omega_1}{\Omega}\sin(\Omega t_{90}) n_y^2 [\sin^2\alpha_{\mathcal{B}} - n_z^2(1-\cos\alpha_{\mathcal{B}})^2] - \frac{1}{2}\frac{\omega_1}{\Omega}\frac{\Delta\omega_0}{\Omega}[1-\cos(\Omega t_{90})] n_y^2 n_z \times \sin\alpha_{\mathcal{B}}(1-\cos\alpha_{\mathcal{B}}) \quad [45]$$

$$b_4 = \frac{1}{2}\frac{\omega_1}{\Omega}\sin(\Omega t_{90}) n_y^2 [-\sin^2\alpha_{\mathcal{B}} + n_z^2(1-\cos\alpha_{\mathcal{B}})^2] + \frac{\omega_1}{\Omega}\frac{\Delta\omega_0}{\Omega}[1-\cos(\Omega t_{90})] n_y^2 n_z \times \sin\alpha_{\mathcal{B}}(1-\cos\alpha_{\mathcal{B}}) \quad [46]$$

$$b_5 = \frac{1}{4}\frac{\omega_1}{\Omega}\sin(\Omega t_{90}) n_y^2 [\sin^2\alpha_{\mathcal{B}} - n_z^2(1-\cos\alpha_{\mathcal{B}})^2] + \frac{1}{2}\frac{\omega_1}{\Omega}\frac{\Delta\omega_0}{\Omega}[1-\cos(\Omega t_{90})] n_y^2 n_z \times \sin\alpha_{\mathcal{B}}(1-\cos\alpha_{\mathcal{B}}) \quad [47]$$

$$b_6 = \frac{1}{4}\frac{\omega_1}{\Omega}\sin(\Omega t_{90})[n_z^4(1-\cos\alpha_{\mathcal{B}})^2 + (1+\cos\alpha_{\mathcal{B}})^2 - 6 n_z^2 \sin^2\alpha_{\mathcal{B}}] - \frac{\omega_1}{\Omega}\frac{\Delta\omega_0}{\Omega}[1-\cos(\Omega t_{90})] n_z \times \sin\alpha_{\mathcal{B}}[(1+\cos\alpha_{\mathcal{B}}) - n_z^2(1-\cos\alpha_{\mathcal{B}})]. \quad [48]$$

Note that a_1, b_1, and b_2 do not depend on the echo spacing. The terms a_1 and b_1 give the contributions from the standard Hahn echoes; the term b_2 is due to the stimulated echo.

For $D_0 = 0$, the expression for the magnetization for the first and second echoes reduces to $\sum_{i=1}^{2} a_i$ and $\sum_{i=1}^{6} b_i$, respectively. These sums are identical to Eq. [11] for $N = 1$ and 2, respectively.

ACKNOWLEDGMENTS

We thank P. Sen, A. Sezginer, R. Kleinberg, and D. Freed for discussions and advice. R. Freedman performed the CPMG measurements with variable echo spacings.

REFERENCES

1. R. L. Kleinberg. "Encyclopedia of Nuclear Magnetic Resonance," Vol. 8, Ch. Well logging, pp. 4960–4969, Wiley, Chichester (1996).
2. G. Eidmann, R. Savelsberg, P. Blümler, and B. Blümich. The NMR MOUSE, a mobile universal surface explorer. *J. Magn. Reson. A* **122,** 104–109 (1996).
3. J. B. Miller and A. N. Garroway. Planar imaging by NMR, *in* "35th Experimental NMR Conference," pp. 186, Pacific Grove, CA (1994).
4. P. J. McDonald. Stray field magnetic resonance imaging. *Prog. Nucl. Magn. Reson. Spectrosc.* **30,** 69–99 (1997).
5. T. N. Rudakov, A. V. Belyakov, and V. T. Mikhaltsevich. A low-frequency instrument for remote nuclear quadrupole resonance experiments. *Meas. Sci. Technol.* **8,** 444–448 (1997).
6. J. P. Yesinowski, M. L. Buess, A. N. Garroway, M. Ziegeweid, and A. Pines. Detection of ^{14}N and ^{35}Cl in cocaine base and hydrochloride using NQR, NMR and SQUID techniques. *Anal. Chem.* **67,** 2256–2263 (1995).

7. H. Y. Carr and E. M. Purcell. Effects of diffusion on free precession in nuclear magnetic resonance experiments. *Phys. Rev.* **94,** 630–638 (1954).
8. S. Meiboom and D. Gill. Modified spin-echo method for measuring nuclear relaxation times. *Rev. Sci. Instrum.* **29,** 688–691 (1958).
9. R. L. Vold, R. R. Vold, and H. E. Simon. Errors in measurements of transverse relaxation rates. *J. Magn. Reson.* **11,** 283–298 (1973).
10. T. E. Bull. Effect of rf field inhomogeneities on spin-echo measurements. *Rev. Sci. Instrum.* **45,** 232–242 (1974).
11. T. B. Benson and P. J. McDonald. Profile amplitude modulation in stray-field magnetic-resonance imaging. *J. Magn. Reson. A* **112,** 17–23 (1995).
12. T. B. Benson and P. J. McDonald. The application of spin echoes to stray-field imaging. *J. Magn. Reson. B* **109,** 314–317 (1995).
13. G. Goelman and M. G. Prammer. The CPMG pulse sequence in strong magnetic field gradients with applications to oil-well logging. *J. Magn. Reson. A* **113,** 11–18 (1995).
14. A. D. Bain and E. W. Randall. Hahn spin echoes in large static gradients following a series of 90° pulses. *J. Magn. Reson. A* **123,** 49–55 (1996).
15. R. Ernst, G. Bodenhausen, and A. Wokaun. "Principles of Nuclear Magnetic Resonance in One and Two Dimensions," Clarendon, Oxford (1987).
16. D. I. Hoult and R. E. Richards. The signal-to-noise ratio of the nuclear magnetic resonance experiment. *J. Magn. Reson.* **24,** 71–85 (1976).
17. R. L. Kleinberg, A. Sezginer, D. D. Griffin, and M. Fukuhara. Novel NMR apparatus for investigating an external sample. *J. Magn. Reson.* **97,** 466–485 (1992).
18. A. A. Maudsley. Modified Carr–Purcell–Meiboom–Gill sequence for NMR Fourier imaging applications. *J. Magn. Reson.* **69,** 488–491 (1986).
19. A. J. Shaka, S. P. Rucker, and A. Pines. Iterative Carr–Purcell trains. *J. Magn. Reson.* **77,** 606–611 (1988).
20. T. Gullion, D. B. Baker, and M. S. Conradi. New, compensated Carr–Purcell sequences. *J. Magn. Reson.* **89,** 479–484 (1990).
21. T. Gullion. The effect of amplitude imbalance on compensated Carr–Purcell sequences. *J. Magn. Reson. A* **101,** 320–323 (1993).
22. C. Counsell, M. H. Levitt, and R. R. Ernst. Analytical theory of composite pulses. *J. Magn. Reson.* **63,** 133–141 (1985).
23. J. D. Ellett, M. G. Gibby, U. Haeberlen, L. M. Huber, M. Mehring, A. Pines, and J. S. Waugh. Spectrometer for multiple-pulse NMR. *Adv. Magn. Reson.* **5,** 117–176 (1971).
24. M. Mehring and J. S. Waugh. Phase transients in pulsed NMR spectrometers. *Rev. Sci. Instrum.* **43,** 649–653 (1972).
25. D. G. Hughes and G. Lindblom. Baseline drift in the Carr–Purcell–Meiboom–Gill pulsed NMR experiment. *J. Magn. Reson.* **13,** 142–147 (1974).
26. D. G. Hughes and G. Lindblom. Baseline drift in the Carr–Purcell–Meiboom–Gill pulsed NMR experiment. *J. Magn. Reson.* **26,** 469–479 (1977).
27. R. R. Ernst and W. A. Anderson. Application of Fourier transform spectroscopy to magnetic resonance. *Rev. Sci. Instrum.* **37,** 93–102 (1966).
28. P. Waldstein and W. E. Wallace. Driven equilibrium methods for enhancement of nuclear transients. *Rev. Sci. Instrum.* **42,** 437–440 (1971).
29. R. Kimmich. "NMR: Tomography, Diffusometry, Relaxometry." Springer-Verlag, Berlin (1997).
30. A. Sezginer, D. D. Griffin, R. L. Kleinberg, M. Fukuhara, and D. G. Dudley. RF sensor of a novel NMR apparatus. *J. Electromagn. Waves Appl.* **7,** 13–30 (1993).
31. D. E. Woessner. Effects of diffusion in nuclear magnetic resonance spin-echo experiments. *J. Chem. Phys.* **34,** 2057–2061 (1961).
32. H. C. Torrey. Bloch equations with diffusion terms. *Phys. Rev.* **104,** 563–565 (1956).
33. R. Kaiser, E. Bartholdi, and R. R. Ernst. Diffusion and field-gradient effects in NMR Fourier spectroscopy. *J. Chem. Phys.* **60,** 2966–2979 (1974).
34. E. J. Fordham, A. Sezginer, and L. D. Hall. Imaging multiexponential relaxation in the (y, $\log_e T_1$) plane, with application to clay filtration in rock cores. *J. Magn. Reson. A* **113,** 139–150 (1995).
35. M. D. Hürlimann. Effective gradients in porous media due to susceptibility differences. *J. Magn. Reson.* **131,** 232–240 (1998).
36. M. D. Hürlimann, K. G. Helmer, T. M. de Swiet, P. N. Sen, and C. H. Sotak. Spin echoes in a constant gradient and in the presence of simple restriction. *J. Magn. Reson. A* **113,** 260–264 (1995).
37. J. D. Jackson. "Classical Electrodynamics," Wiley, New York (1975).